

# Constructing helical edge states with two-dimensional $C_6$ and $C_6$ -like symmetric photonic crystals

Xiaolong Wang <sup>1,\*</sup> Wenjie Sui <sup>1,\*</sup> Yu Zhang <sup>1</sup> Zirui Zhang <sup>1</sup> Yongxi Yao <sup>1</sup> Xinqi Meng <sup>1</sup> Hongfang Zhang <sup>1,2</sup>  
Yujing Wang <sup>3</sup> and Bing Yang <sup>1,2,†</sup>

<sup>1</sup>School of Physical Science and Information Engineering, Liaocheng University, Liaocheng 252059, China

<sup>2</sup>Shandong Provincial Key Laboratory of Optical Communication Science and Technology, Liaocheng 252059, China

<sup>3</sup>School of Communications and Information Engineering, Nanjing University of Posts and Telecommunications, Nanjing 210003, China



(Received 4 October 2023; revised 17 May 2024; accepted 20 May 2024; published 31 May 2024)

In recent years, helical edge states (HESs) in two-dimensional (2D) topological pseudospin photonic crystals (PhCs) have attracted more and more attention due to their pseudospin-locked unidirectional propagation of electromagnetic (EM) waves. Most of the studies are based on a kind of triangular lattice PhCs with the primitive cell containing six identical scatterers with  $C_6$  symmetry. By shrinking or expanding the six-scatterer structure in the primitive cell, topological pseudospin PhCs are formed and HESs can be constructed along the zigzag interface of two PhCs with distinct topological pseudospins. In this paper, based on several 2D  $C_6$  symmetric dielectric PhCs with the primitive cell containing different shapes of regular polygon prisms, we design  $C_6$ -like symmetric PhCs by partially replacing regular polygon prisms in the primitive cell of  $C_6$  symmetric PhCs. Numerical calculations show all these different PhCs can possess similar band structures by tuning sizes of the prisms even in the  $C_6$ -like symmetric PhCs in which the  $C_6$  symmetry is lacking. Then, by splicing these  $C_6$  and  $C_6$ -like symmetric PhCs along their zigzag interfaces, we construct the similar HESs. Through calculating the energy propagation of these HESs, we demonstrate their same unidirectional propagation properties and the similar immunity to corners and defects along the interface. Our results indicate that the formation and the property of HESs in 2D topological pseudospin PhCs are only determined by the topological band structures and the topological pseudospins of PhCs on both sides of the interface, rather than the shapes of the scatterers in PhCs in real space. Our study provides further understanding on the formation of HESs and paves the way for control of topological edge states in practice.

DOI: [10.1103/PhysRevB.109.195305](https://doi.org/10.1103/PhysRevB.109.195305)

## I. INTRODUCTION

Topological photonics has been a hot research field in recent years [1–8]. Similar to the topological states in condensed matter physics [9,10], researchers have also found and designed photonic topological states (PTSs) such as photonic quantum Hall states [11–16], photonic quantum spin Hall states [17–20], and photonic valley Hall states in optical systems [21–25]. Due to the topological protection, PTSs have some excellent properties for electromagnetic (EM) wave propagation, such as unidirectionality without backscattering and defect immunity [26–29], which makes PTSs potentially valuable for optical computing and optical communication [30–37].

PTSs were first realized in magneto-optical materials by breaking time-reversal symmetry to construct chiral edge states similar to the quantum Hall effect [12]. However, due to the weak magneto-optical response in the optical frequency and the loss of magneto-optical materials, the PTSs in magneto-optical materials can hardly be applied in optical fields [38]. Therefore, other types of PTSs have been proposed and designed, such as pseudospin protected PTSs in coupled ring waveguides [14], Floquet PTSs in

waveguide arrays [39–41], and PTSs in bianisotropic materials [19].

Among these PTSs, a kind of pseudospin PTSs based on  $C_6$  symmetric photonic crystals (PhCs) proposed by Wu and Hu has attracted wide attentions due to their simple structure, all-dielectric design, and easy integration with current photonic devices [18]. In a two-dimensional (2D) triangular lattice PhC, they design band gaps with different topological pseudospins by shrinking or expanding the distance of six scatterers away from the center of the primitive cell. By splicing two PhCs with different pseudospins, they construct topologically protected helical edge states (HESs) within the common band gaps of two PhCs [18]. So far, many  $C_6$  symmetric PhC structures have been designed, and this kind of pseudospin protected HES has also been observed in experiment [42,43]. However, most of the studies are based on the same PhC structures containing six identical scatterers in the primitive cell, and researchers construct the HESs and investigate their topological properties by shrinking/expanding the six-scatterer structure in the primitive cell in which the  $C_6$  symmetry is always maintained [44–46]. So, a question arises. Does this kind of HES still exist if the PhC lacks the  $C_6$  symmetry? Or rather, what is the effect of real space structures of PhCs on the HESs? As far as we know, there is no research on this issue up to now. But it is very important to further understand the formation of HESs in theory and to design PTSs in practice.

\*These authors contributed equally to this work.

†Corresponding author: yangbing@lcu.edu.cn

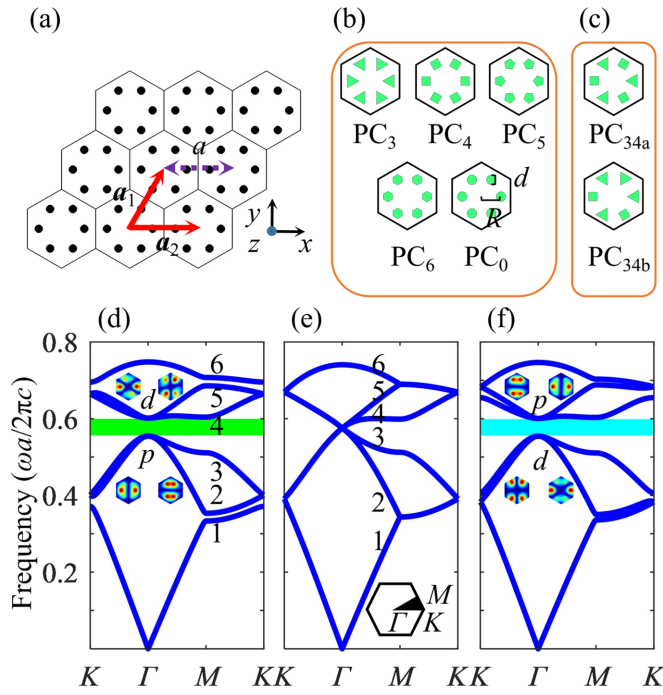


FIG. 1. (a) Periodic structure of the PhCs. (b) Primitive cells of five  $C_6$  symmetric PhCs. (c) Primitive cells of two  $C_6$ -like symmetric PhCs. (d)–(f) Frequency bands of  $PC_0$  as  $R = a/3 - 0.03a$ ,  $a/3$ , and  $a/3 + 0.025a$ , respectively, with  $d = a/6$ . Inset in (e) is the first BZ and insets in (d) and (f) show the  $|E_z|$  fields of  $p$  and  $d$  orbitals at the  $\Gamma$  point.

In this paper, we first design several different configurations of 2D  $C_6$  symmetric dielectric PhCs in which the scatterers are regular triangular prisms, regular quadrangular prisms, regular pentagonal prisms, regular hexagonal prisms, and cylinders, respectively. And then by partially replacing the scatterers in the primitive cell of these  $C_6$  symmetric PhCs, we design  $C_6$ -like symmetric PhCs without  $C_6$  symmetry. By adjusting sizes of the scatterers and shrinking/expanding the six-scatterer structure in the primitive cell, we construct almost the same band structures with the same topological properties in each of these  $C_6$  and  $C_6$ -like symmetric PhCs. By splicing these PhCs along their zigzag interface, we demonstrate that the similar HESs can be constructed using either  $C_6$  or  $C_6$ -like symmetric PhCs, and these HESs have the same unidirectional propagations and similar immunity to corners and defects along the interface for EM waves propagation.

The rest of the paper is arranged as follows. In Sec. II, we introduce the theoretical model and topological properties of our models. In Sec. III, the numerical results and discussions are presented. A summary is given in Sec. IV.

## II. MODELS AND TOPOLOGICAL PROPERTIES OF BAND GAPS

Our model is based on a 2D triangular lattice PhC, as shown in Figs. 1(a)–1(c). Figure 1(a) shows the periodic structure with  $\mathbf{a}_1$  and  $\mathbf{a}_2$  being the lattice vectors,  $a$  being the lattice constant, and black dots representing positions of scatterers in the primitive cell. Figure 1(b) shows the primitive cells as the

scatterers are regular triangular prisms, regular quadrangular prisms, regular pentagonal prisms, regular hexagonal prisms, and cylinders. Correspondingly we label these  $C_6$  symmetric PhCs in Fig. 1(b) as  $PC_3$ ,  $PC_4$ ,  $PC_5$ ,  $PC_6$ , and  $PC_0$ , respectively. As some scatterers in the primitive cell of these  $C_6$  symmetric PhCs are replaced by other types of scatterers, the  $C_6$  symmetry is broken, and we call them  $C_6$ -like symmetric PhCs. For examples, in Fig. 1(c) we show two  $C_6$ -like symmetric PhC primitive cells in which three/two regular triangular prisms are replaced by regular quadrangular prisms. We label these two  $C_6$ -like symmetric PhCs as  $PC_{34a}$  and  $PC_{34b}$ , respectively. In Figs. 1(b) and 1(c), the distance between the center of the primitive cell and each scatterer is  $R$ . The diameter of the cylinder is  $d$  and the side length of the prism scatterer is  $l_n$  with  $n$  being the number of prismatic edges. The relative permittivity of dielectric scatterers (air background) is  $\epsilon_r = 11.7$  ( $\epsilon_A = 1$ ) and the TM modes with an electric field along the  $z$  direction are considered. In our studies, the calculation of band structures and the full wave simulations of an EM wave are performed with COMSOL MULTIPHYSICS.

Taking  $PC_0$  as an example, when  $R = a/3$  and  $d = a/6$ , the frequency band of the PhCs is shown in Fig. 1(e) with the numbers labeling bands from low to high. Clearly, the second to the fifth bands form a double degenerate Dirac cone around the  $\Gamma$  point in the first Brillouin zone (BZ). Based on the PhCs in Fig. 1(e), by decreasing or increasing the values of  $R$ , the Dirac cone can be opened. Figures 1(d) and 1(f) are the corresponding frequency bands for  $R = a/3 - 0.03a$  and  $R = a/3 + 0.025a$ , respectively. Here,  $\omega a/2\pi c$  is the reduced frequency with  $\omega$  being the angular frequency and  $c$  being the speed of light in vacuum. In the insets in Figs. 1(d) and 1(f), we show the two pairs of orthogonal eigenfields of  $|E_z|$  at the degenerate frequencies at  $\Gamma$  in the BZ, where the dipole states and the quadrupole states correspond to the  $p$  orbital ( $p_x, p_y$ ) and  $d$  orbital ( $d_{xy}$  and  $d_{x^2-y^2}$ ) field distributions, respectively.

The topological properties of the band gaps in Figs. 1(d) and 1(f) can be understood based on the  $\mathbf{k} \cdot \mathbf{p}$  theory. Constructing pseudospin states as  $p_{\pm} = (p_x \pm ip_y)/\sqrt{2}$  and  $d_{\pm} = (d_{x^2-y^2} \pm id_{xy})/\sqrt{2}$ , and taking  $(p_+, d_+, p_-, d_-)$  as the basis functions, the effective Hamiltonian near the  $\Gamma$  point in the BZ can be expressed as

$$H^{\text{eff}}(k) = \begin{pmatrix} M - Bk^2 & Ak_+ & 0 & 0 \\ A^*k_- & -M + Bk^2 & 0 & 0 \\ 0 & 0 & M - Bk^2 & A^*k_- \\ 0 & 0 & A^*k_+ & -M + Bk^2 \end{pmatrix}. \quad (1)$$

Here,  $M = (\epsilon_d^0 - \epsilon_p^0)/2$  with  $\epsilon_d^0$  and  $\epsilon_p^0$  being the frequencies of the  $d$  orbitals and  $p$  orbitals at the  $\Gamma$  point, respectively.  $k_{\pm} = k_x \pm ik_y$  and coefficient  $A$  ( $B$ ) originates from the first-order (second-order) perturbation among  $p_x, p_y, d_{xy}$ , and  $d_{x^2-y^2}$ . Equation (1) has a similar form as the effective Hamiltonian of the CdTe/HgTe/CdTe quantum well in the Bernevig-Hughes-Zhang model [47]. So, we can obtain the spin Chern number of the PhCs as

$$C_{\pm} = \pm \frac{1}{2} [\text{sgn}(M) + \text{sgn}(B)]. \quad (2)$$

For the PhCs with  $p$  orbitals lower than  $d$  orbitals at the  $\Gamma$  point,  $M > 0$  and  $B < 0$ , then  $C_{\pm} = 0$  and the corresponding

band gap is trivial. For the PhCs with  $p$  orbitals higher than  $d$  orbitals,  $M < 0$  and  $B < 0$ , then  $C_{\pm} = \mp 1$  and the corresponding band gap is topologically nontrivial. In Fig. 1(d), the second and third (fourth and fifth) bands at the  $\Gamma$  point form degenerate  $p$  ( $d$ ) orbitals, and  $p$  orbitals are lower than  $d$  orbitals, so the band gap is trivial, shown as the green region. While in Fig. 1(f), the second and third (fourth and fifth) bands form degenerate  $d$  ( $p$ ) orbitals at the  $\Gamma$  point and the  $p$  orbitals are higher than the  $d$  orbitals, so the band gap is topologically nontrivial, shown as the cyan region [48]. With Eq. (2), we can recognize the topological properties of the  $PC_0$  PhCs just with the relative positions of  $p$  orbitals and  $d$  orbitals at the  $\Gamma$  point in the BZ [42,44,49].

For the  $C_6$  symmetric PhCs with scatterers being regular triangular prisms, regular quadrangular prisms, regular pentagonal prisms, and regular hexagonal prisms, by tuning the sizes of those polygonal prisms, we can get their band structures with the same configurations and the same topological properties as those shown in Figs. 1(d)–1(f) (see the Supplemental Material [50]). For the  $C_6$ -like symmetric PhCs, although the systems lack the  $C_6$  rotational symmetry, our calculations reveal that their frequency bands exhibit similar configurations and the same topological properties as those of the PhCs with  $C_6$  symmetry (see the Supplemental Material [50]). It is worth noting that to get similar band structures of the  $C_6$  symmetric and  $C_6$ -like symmetric PhCs, we tune the sizes of the different regular polygonal prisms to obtain the same scattering effects of EM waves during constructions of these PhCs. And moreover, based on the tight-binding model, we also give our theoretical analysis of the band structures and topological properties of the PhCs in which different kinds of scatterers are included (see the Supplemental Material [50]). Also, we note that due to the breaking of the  $C_6$  symmetry in  $C_6$ -like symmetric PhCs in  $PC_{34a}$  and  $PC_{34b}$ , the two  $d$  ( $p$ ) orbitals at the  $\Gamma$  point are not exactly degenerate. However, in our studies, these kinds of separations of two  $d$  ( $p$ ) orbitals at the  $\Gamma$  point are so small that they cannot even be observed (see the Supplemental Material [50]). So, in our description in the following work, we do not distinguish these small separations and still call them degenerate  $d$  ( $p$ ) orbitals, and Eq. (2) is still effective for the qualitative descriptions for the topological properties of the PhCs in our studies [42,44,49].

### III. RESULTS AND DISCUSSION

#### A. Variations of topological band gaps in $C_6$ and $C_6$ -like PhCs

To construct HESs at the interface of PhCs, we first calculate the band structures of PhCs in Figs. 1(b) and 1(c) and display their topological band gaps as  $R$  changes around  $R = a/3$  in Fig. 2. It should be noted that we adjust the side length  $l_n$  of each scatterer in our models to ensure that frequencies of the fourfold degenerate Dirac points at  $R = a/3$  are the same as that in Fig. 1(e). In Fig. 2, the solid and the dash-dotted lines (the dashed and dotted lines) mark the frequencies of the band gap top (bottom) at the  $\Gamma$  and  $M$  points in the BZ, respectively. The red, blue, green, magenta, black, yellow, and cyan lines correspond to the PhCs of  $PC_3$ ,  $PC_4$ ,  $PC_5$ ,  $PC_6$ ,  $PC_0$ ,  $PC_{34a}$ , and  $PC_{34b}$ , and the yellow and the blue regions mark the topologically trivial and nontrivial complete

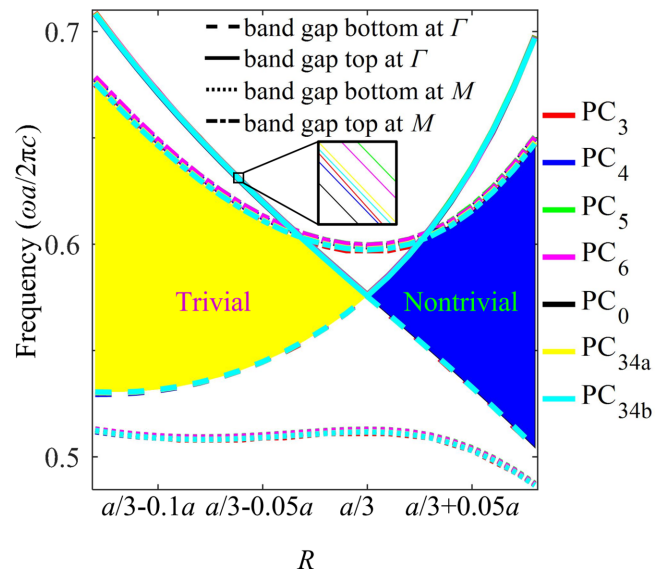


FIG. 2. Variations of topological band gaps in  $C_6$  and  $C_6$ -like PhCs. The solid and the dash-dotted lines (the dashed and dotted lines) denote frequencies of the band gap top (bottom) at the  $\Gamma$  and  $M$  points in the BZ, respectively. The red, blue, green, magenta, black, yellow, and cyan lines correspond to the PhCs of  $PC_3$ ,  $PC_4$ ,  $PC_5$ ,  $PC_6$ ,  $PC_0$ ,  $PC_{34a}$ , and  $PC_{34b}$ , respectively. The inset shows the localized magnification of these bands.

band gaps, respectively. From Fig. 2, we can see that for all the PhCs, increasing/decreasing  $R$  from  $R = a/3$  can open the band gaps at the  $\Gamma$  point. Moreover, as  $R$  changes, the variations of band gaps of these PhCs exhibit almost identical configurations and the same topological properties. The inset shows the localized magnification of these bands, denoting the little difference of frequencies of these PhCs.

#### B. Constructing HESs with $C_6$ symmetric PhCs

For ease of description in the following text, we define some abbreviation rules. Firstly, the PhCs with topologically trivial (nontrivial) band gaps are denoted with  $T$  ( $N$ ) PhCs. Secondly, if the primitive cell of PhCs only contains regular  $n$ -gon prisms ( $n = 3, 4, 5, 6$ , or  $0$ ), the structure is abbreviated as  $T_n$  or  $N_n$  PhCs, with  $n = 0$  corresponding to cylinder scatterer. If the primitive cell contains multiple types of scatterers, then the structure is abbreviated as  $T_{n_1 n_2 \dots n_m}$  or  $N_{n_1 n_2 \dots n_m}$  PhCs, with  $n_1, n_2, \dots, n_m$  indicating shapes of the scatterers, independent of their numbers and arrangements in the primitive cell. For example, both the PhCs shown in Fig. 1(c) can be represented with  $T_{34}$  ( $N_{34}$ ) for the topologically trivial (nontrivial) cases with  $R < a/3$  ( $R > a/3$ ). Correspondingly, interface structures constructed with different PhCs are abbreviated as  $T_n$ - $N_n$  or  $T_{n_1 n_2 \dots n_m}$ - $N_{n_1 n_2 \dots n_m}$  interface.

For the  $C_6$  symmetric PhCs  $T_n$  and  $N_n$ , topologically protected HESs can be formed at  $T_n$ - $N_n$  interfaces. Figures 3(a) and 3(b) show the projected band diagrams of  $T_3$ - $N_3$  and  $T_4$ - $N_4$  zigzag interfaces, in which the gray regions denote bulk states, and the red curves are HESs. The insets in Figs. 3(a) and 3(b) respectively show the supercells used to calculate the projected band diagrams with blue lines denoting the zigzag interfaces. The upper (lower) part of the interface is the  $T$  ( $N$ )

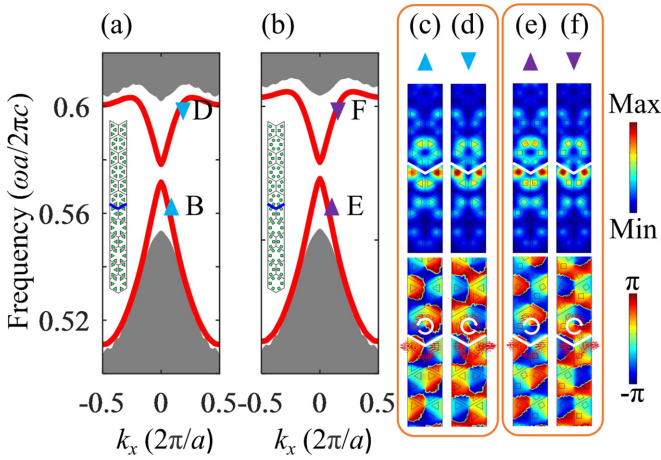


FIG. 3. (a), (b) Projected band diagram of the  $T_3$ - $N_3$  and  $T_4$ - $N_4$  zigzag interfaces with shaded areas denoting bulk states and red curves denoting HESs. Insets in (a) and (b) show the supercells for calculations. (c)–(f) The eigenfield modes  $|E_z|$  (upper panels) and phase distributions  $\phi = \arg(E_z)$  (lower panels) of HESs at  $B$ ,  $D$ ,  $E$ , and  $F$  in (a) and (b), respectively.

PhCs with  $R = a/3 - 0.03a$  ( $R = a/3 + 0.025a$ ). It can be seen from Figs. 3(a) and 3(b) that the HESs appear at the interfaces of these two  $T_n$ - $N_n$  structures, and these HESs have the same configurations with upper and lower branches with a small gap in between. These results are consistent with the research in Ref. [18].

We choose two HESs at points  $B$  and  $D$  denoted with triangles in Fig. 3(a) to give exemplifications. Point  $B$  ( $D$ ) is on the lower (upper) branch of HESs with  $k_x = 0.12\pi/a$  ( $k_x = 0.32\pi/a$ ) and its eigenfield mode  $|E_z|$  and phase distribution  $\phi = \arg(E_z)$  are shown in Fig. 3(c) [Fig. 3(d)] with the white lines denoting the zigzag interfaces. From the  $|E_z|$  distributions shown in the upper panels in Figs. 3(c) and 3(d), we can see that these HESs are indeed localized near the interface. From the phase distributions  $\phi = \arg(E_z)$  shown in the lower panels in Figs. 3(c) and 3(d), we can see that the directions of the phase vortex at points  $B$  and  $D$  are counterclockwise and clockwise, respectively, as shown by the white circular arrows in the panels. Different phase vortex directions denote the opposite pseudospin feature. In the following, we denote the phase vortices of  $B$  and  $D$  as the pseudospin-up and pseudospin-down, respectively. Together with the unidirectional propagation of the Poynting vectors marked with the red arrows in phase distributions, we can clearly see the pseudospin-locked unidirectional propagation of the HESs along these interfaces.

Figures 3(e) and 3(f) show the results of the  $|E_z|$  fields (upper panels) and phase distributions  $\phi = \arg(E_z)$  (lower panels) of the corresponding HESs at  $E$  and  $F$  with  $k_x = 0.12\pi/a$  and  $k_x = 0.32\pi/a$  in Fig. 3(b), respectively. It can be seen that both the  $|E_z|$  fields and the phase distributions  $\phi = \arg(E_z)$  have the same characteristics as those in Figs. 3(c) and 3(d). For the  $T_5$ - $N_5$ ,  $T_6$ - $N_6$ , and  $T_0$ - $N_0$  interface structures, the similar projected edge states,  $|E_z|$  distributions, and the phase distributions  $\phi = \arg(E_z)$  can also be obtained as those in Fig. 3 (see the Supplemental Material [50]).

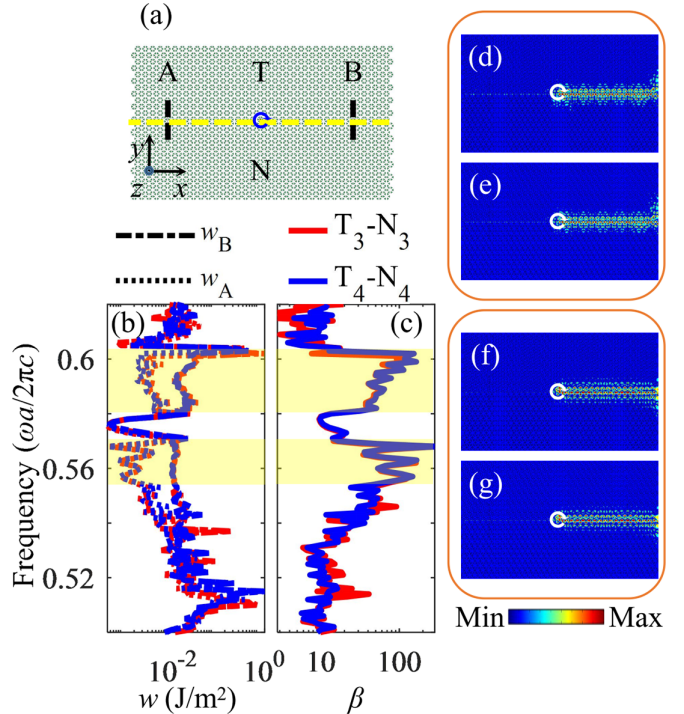


FIG. 4. (a) Schematic plot of the calculation model. The upper (lower) side of the interface is  $T$  ( $N$ ) PhCs with interface marked with a yellow dashed line, and the pseudospin-down vortex source is a magnetic dipole shown by the blue circular arrow. Vertical dotted lines  $A$  and  $B$  are used to calculate the energy propagation of  $w_A$  and  $w_B$ . (b), (c) Unidirectional propagation of the HESs stimulated by vortex sources along the interface in the  $T_3$ - $N_3$  and  $T_4$ - $N_4$  structures. (d), (e) [(f), (g)] Simulations of the propagation of the HESs stimulated by pseudospin-down vortex source with frequency at points  $D$  and  $F$  ( $B$  and  $E$ ) in Figs. 3(a) and 3(b), respectively.

To characterize the unidirectional propagation of the HESs constructed above, we calculate the energy propagation of the EM waves along the interface. The calculation model is shown in Fig. 4(a) in which the upper (lower) side of the interface is  $T$  ( $N$ ) PhCs, the interface is marked with a yellow dashed line, and the vortex source is denoted with the blue circular arrow. In the following, we choose a magnetic dipole with a pseudospin-down feature as the vortex source for our study. We calculate the time-averaged energy  $w_A$  and  $w_B$  through two cut lines denoted by  $A$  and  $B$  denoted with vertical dotted lines in the figure. Here, both  $A$  and  $B$  are  $10\sqrt{3}a/3$  long in the  $y$  direction and  $12.5a$  away from the vortex source along the interface. The results for the  $T_3$ - $N_3$  and  $T_4$ - $N_4$  structures are shown in Fig. 4(b) with the dash-dotted (dotted) lines for  $w_B (w_A)$ . Also, we calculate the unidirectional isolation rate to characterize the unidirectionality of the HESs with

$$\beta = 10 \times \lg \frac{w_B}{w_A}. \quad (3)$$

The corresponding results are shown in Fig. 4(c) with a red (blue) line for the  $T_3$ - $N_3$  ( $T_4$ - $N_4$ ) interface structure. The yellow backgrounds in Figs. 4(b) and 4(c) mark the frequency range of the HESs. It can be seen that no matter in the  $T_3$ - $N_3$  or the  $T_4$ - $N_4$  structure, the values of  $w_B$  are much larger than  $w_A$  and the unidirectional isolation rate  $\beta$  is greater than

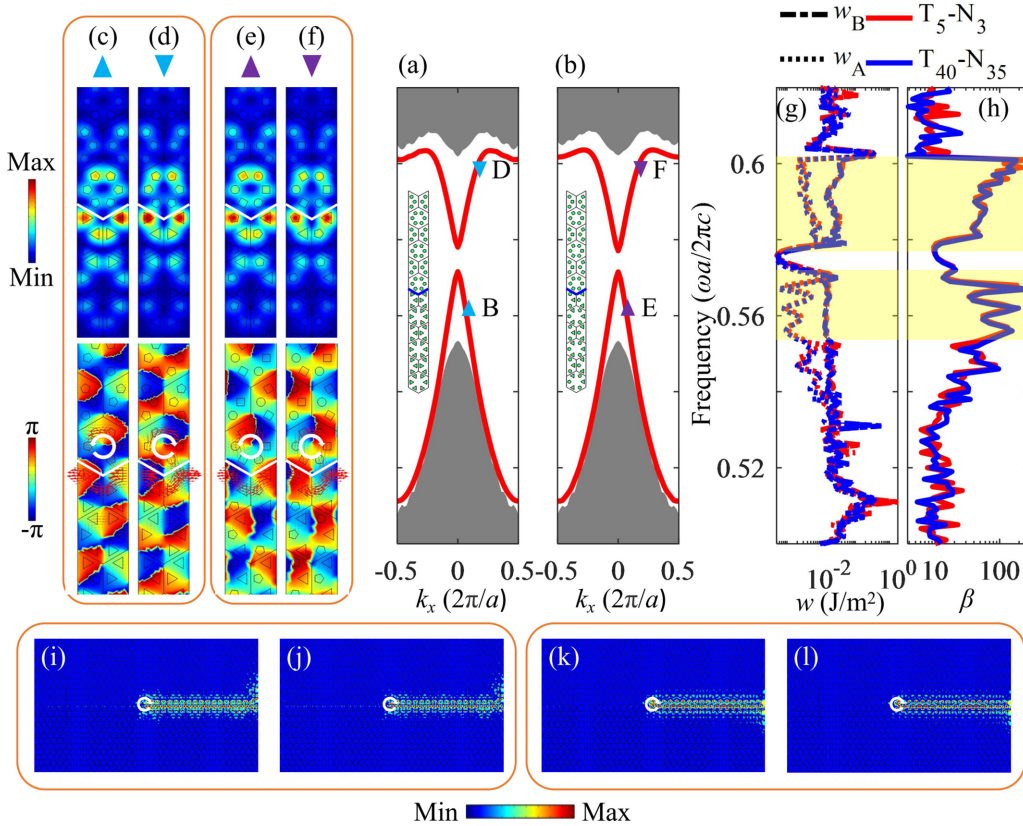


FIG. 5. (a), (b) Projected band diagram of the  $T_5\text{-}N_3$  and  $T_{40}\text{-}N_{35}$  interfaces with shaded areas denoting bulk states and red curves denoting HESs. Insets show the supercells for calculations. (c)–(f) The eigenfield modes  $|E_z|$  (upper panels) and phase distributions  $\phi = \arg(E_z)$  (lower panels) of HESs at  $B$ ,  $D$ ,  $E$ , and  $F$  in (a) and (b), respectively. (g), (h) Unidirectional propagation of the HESs stimulated by pseudospin-down vortex sources along the interface in the  $T_5\text{-}N_3$  and  $T_{40}\text{-}N_{35}$  structures. (i), (j) [(k), (l)] Simulations of the propagation of the HESs stimulated by pseudospin-down vortex sources with frequency at points  $D$  and  $F$  ( $B$  and  $E$ ) in (a) and (b), respectively.

10 dB within the frequency range of HESs, indicating the pseudospin-locked EM wave unidirectional propagation to the right along the interface. Moreover, although the scatterers are different in  $T_3\text{-}N_3$  and  $T_4\text{-}N_4$  structures, their results of  $w_A$ ,  $w_B$ , and  $\beta$  almost take the same values within the frequency range of HESs.

Figures 4(d) and 4(e) [Figs. 4(f) and 4(g)] show the simulation results of the wave propagation of the HESs stimulated by the pseudospin-down vortex sources with frequency at points  $D$  and  $F$  ( $B$  and  $E$ ) in Figs. 3(a) and 3(b), respectively. Obviously, the pseudospin-locked EM waves are excited and propagate unidirectionally in both cases. Here, it is worth noting that for the frequency at points  $D$  and  $F$  at the upper branch of the HESs, due to the pseudospin-down features of  $D$  and  $F$  coinciding with the pseudospins of vortex sources, the HESs of  $D$  and  $F$  are excited. However, for the frequency at points  $B$  and  $E$  at the lower branch of the HESs, the pseudospin-up features of points  $B$  and  $E$  are opposite to the pseudospins of vortex sources, so the time-reversal symmetry pairs of  $B$  and  $E$  at  $k_x = -0.12\pi/a$  are excited in the simulations, and the excited EM waves also propagate to the right along the interface. From the results in Figs. 3 and 4, we deduce that the unidirectional propagations of HESs are determined by the configurations of edge states and are not related to the shapes of scatterers in the PhCs on both sides of the interface. We further confirm this conclusion by per-

forming the same calculations for the  $T_5\text{-}N_5$ ,  $T_6\text{-}N_6$ , and  $T_0\text{-}N_0$  interface structures (see the Supplemental Material [50]).

### C. Constructing HESs with $C_6$ and $C_6$ -like symmetric PhCs

The above studies concentrate on the interface structures in which both  $T$  and  $N$  PhCs contain the same scatterers. In this section, we consider the interface structures in which the PhCs on both sides of the interface contain different scatterers. Without loss of generality, we calculate projected band diagrams of the  $T_5\text{-}N_3$  and  $T_{40}\text{-}N_{35}$  structures. The results are shown in Figs. 5(a) and 5(b) with the calculation supercells shown in the insets in each panel. From Figs. 5(a) and 5(b), we can see that the HESs appear at the interfaces of these two structures, and these HESs have the same configurations and the same frequencies as those in Figs. 3(a) and 3(b).

In the same way, we choose two HESs at points  $B$  and  $D$  denoted with triangles in Fig. 5(a) to give detailed demonstrations. Points  $B$  and  $D$  are at the same positions as states  $B$  and  $D$  ( $E$  and  $F$ ) in Fig. 3(a) [Fig. 3(b)] with  $k_x = 0.12\pi/a$  and  $k_x = 0.32\pi/a$ , respectively. Their eigenfield modes  $|E_z|$  and phase distributions  $\phi = \arg(E_z)$  are shown in Figs. 5(c) and 5(d). Clearly, their results have similar characteristics as the  $|E_z|$  fields and phase distributions  $\phi = \arg(E_z)$  in Figs. 3(c)–3(f). Also, in Figs. 5(e) and 5(f), we give out the  $|E_z|$  fields and phase distributions  $\phi = \arg(E_z)$  of the HESs at points  $E$  and

$F$  in the  $T_{40}-N_{35}$  structure. Obviously, their distributions are almost the same as those in Figs. 5(c) and 5(d), respectively.

For the unidirectional propagation of the HESs in Figs. 5(a) and 5(b), we show the calculation results of  $w_B$  ( $w_A$ ) with dash-dotted (dotted) lines in Fig. 5(g) and the unidirectional isolation ratio  $\beta$  in Fig. 5(h), with the red and the blue lines for the  $T_5-N_3$  and  $T_{40}-N_{35}$  structures, respectively. The yellow backgrounds mark the frequency range of the HESs. We can see that in both the  $T_5-N_3$  and the  $T_{40}-N_{35}$  structures, the values of  $w_B$  are much larger than  $w_A$ , and the unidirectional isolation rate  $\beta$  is greater than 10 dB within the frequency range of HESs. Moreover, despite the different shapes of scatterers in the  $T_5$  and  $N_3$  PhCs in the  $T_5-N_3$  structure, and in the  $T_{40}$  and  $N_{35}$  PhCs in the  $T_{40}-N_{35}$  structure, their results of  $w_A$ ,  $w_B$ , and  $\beta$  almost take the same values within the frequency range of HESs, and all these results are almost the same as those in Figs. 4(b) and 4(c), which indicates that the pseudospin-locked unidirectional propagation of HESs is not related to the shapes of scatterers, but determined by the band structures of the PhCs on both sides of the interface.

Figures 5(i) and 5(j) [Figs. 5(k) and 5(l)] show the simulation results of the propagation of the HESs stimulated by pseudospin-down vortex sources with frequency at points  $D$  and  $F$  ( $B$  and  $E$ ) in Figs. 5(a) and 5(b), respectively. Obviously, the pseudospin-locked EM waves are excited and propagate unidirectionally in both cases. We also carry out the same calculations for the  $T_{345}-N_6$  and  $T_{45603}-N_{365046}$  structures and obtain the same conclusions (see the Supplemental Material [50]).

Based on the above studies, we find that although the  $C_6$  and  $C_6$ -like symmetric PhCs on both sides of the interface contain different shapes of scatterers, their frequency bands can be adjusted to have the same structures with the same topological properties, and the corresponding HESs also have the same configurations and unidirectional propagation of EM waves. So, we conclude that the HESs are only related to the band structures in reciprocal space, and are not related to the real space structures of the PhCs on both sides of the interface.

#### D. Robustness of unidirectional propagation of HESs

To confirm the robustness of the HESs constructed above, we check the unidirectional propagation of the EM waves along the Z-shape zigzag interfaces. The simulation model is shown in the inset in Fig. 6(i) with a blue dashed line denoting the Z-shape interface. The upper (lower) side of the interface is  $T$  ( $N$ ) PhCs and the pseudospin-down vortex source is denoted by the white circular arrow at the interface. The simulation results for the interfaces of  $T_3-N_3$ ,  $T_5-N_3$ ,  $T_{345}-N_6$ , and  $T_{45603}-N_{365046}$  with frequency at HESs of  $B$  and  $E$  are shown in Figs. 6(a)–6(d), respectively. From Figs. 6(a)–6(d), we can see that the excited HESs unidirectionally propagate to the right and pass by two  $60^\circ$  corners without reflections along the interfaces. In Figs. 6(e)–6(h), a scatterer is removed from the interface to form a cavity defect and two adjacent primitive cells of  $T$  and  $N$  PhCs are exchanged to include interface disorder defects at positions denoted with the red dotted circles (enlarged in the inset). It can be seen that the excited HESs in these structures can also pass through the lo-

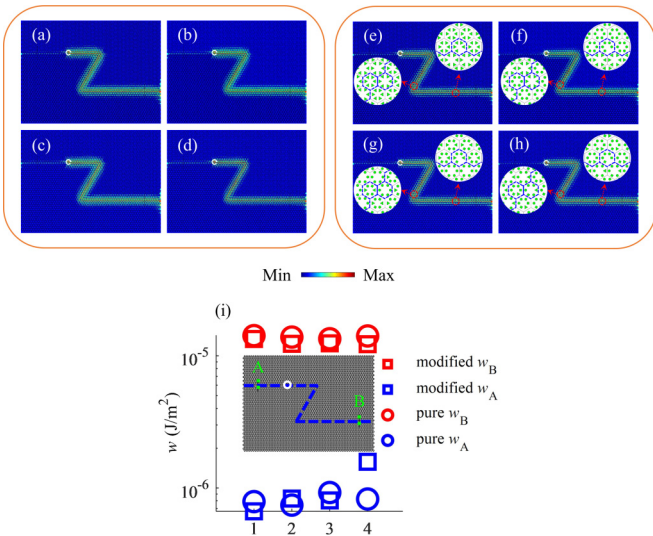


FIG. 6. Robustness of the unidirectional propagation of HESs. (a)–(d) Unidirectional propagation of the HESs along a pure Z-shape interface in the  $T_3-N_3$ ,  $T_5-N_3$ ,  $T_{345}-N_6$ , and  $T_{45603}-N_{365046}$  structures, respectively. (e)–(h) Unidirectional propagation of the HESs along a modified Z-shape interface in  $T_3-N_3$ ,  $T_5-N_3$ ,  $T_{345}-N_6$ , and  $T_{45603}-N_{365046}$  structures, respectively. The cavity defect and disorders are enlarged in the insets. (i) Time average energy  $w_A$  and  $w_B$  through two cut lines  $A$  and  $B$  at Z-shape interfaces with red (blue) markers for  $w_B$  ( $w_A$ ) and circles (squares) for pure Z-shape interfaces without defects (modified Z-shape interfaces with defects). The inset is the calculation model.

cal defects and still maintain their unidirectional propagation without noticeable reflections.

To quantify these unidirectional propagations, time average energies  $w_A$  and  $w_B$  through two cut lines  $A$  and  $B$  indicated by vertical green lines as shown in the inset in Fig. 6(i) are calculated in these Z-shape interfaces. The results are shown in Fig. 6(i) from left to right for the  $T_3-N_3$ ,  $T_5-N_3$ ,  $T_{345}-N_6$ , and  $T_{45603}-N_{365046}$  structures, respectively, with red (blue) markers for  $w_B$  ( $w_A$ ) and circles (squares) for pure Z-shape interfaces without defects (modified Z-shape interfaces with defects). It can be seen that  $w_B$  is always about one order of magnitude larger than  $w_A$ , and  $w_B$  ( $w_A$ ) of pure Z-shape interfaces and modified Z-shape interfaces take almost the same values. These results clearly demonstrate that the constructed HESs with  $C_6$  and  $C_6$ -like PhCs have similar unidirectional propagations with almost the same immunities to corners and defects along interfaces. It is worth noting that due to the very small values of  $w_A$ , it is very easily affected by scattering of the EM waves at the left exit port of the system, as shown by the blue marks in Fig. 6(i).

#### IV. SUMMARY

In this paper, we construct 2D  $C_6$  symmetric PhCs containing different shapes of scatterers and use them to design topologically protected HESs. And, by partially replacing the scatterers in the primitive cell of the  $C_6$  symmetric PhCs, we construct  $C_6$ -like symmetric PhCs and demonstrate that similar topological band structures and HESs can be designed using  $C_6$  symmetric and  $C_6$ -like symmetric PhCs. Our results

reveal that both the configurations of the HESs and their topologically protected unidirectional propagations are determined by the band structures and the topological properties of the PhCs on both sides of the interface and are independent of the real space shapes of the scatterers in the PhCs. Our study provides further understandings on the formations of the HESs and paves the way for control of topological edge states in practice.

## ACKNOWLEDGMENTS

The authors would like to thank Bao Zhao and Zengtao Lv for helpful discussions. This work is supported by the Natural Science Foundations of Shandong Province of China (Grant No. ZR2021MA091), Natural Science Foundations of Liaocheng University (Grant No. 318051705), and the Research Fund from the MOE of China (Grant No. JZW17SL01).

- 
- [1] L. Lu, J. D. Joannopoulos, and M. Soljačić, Topological photonics, *Nat. Photonics* **8**, 821 (2014).
  - [2] X.-C. Sun, C. He, X.-P. Liu, M.-H. Lu, S.-N. Zhu, and Y.-F. Chen, Two-dimensional topological photonic systems, *Prog. Quantum Electron.* **55**, 52 (2017).
  - [3] T. Ozawa *et al.*, Topological photonics, *Rev. Mod. Phys.* **91**, 015006 (2019).
  - [4] M. Kim, Z. Jacob, and J. Rho, Recent advances in 2D, 3D and higher-order topological photonics, *Light: Sci. Appl.* **9**, 130 (2020).
  - [5] M. Segev and M. A. Bandres, Topological photonics: Where do we go from here? *Nanophotonics* **10**, 425 (2020).
  - [6] B. Y. Xie, H. F. Wang, X. Y. Zhu, M. H. Lu, Z. D. Wang, and Y. F. Chen, Photonics meets topology, *Opt. Express* **26**, 24531 (2018).
  - [7] P. Jiang, N. Ma, X. Qiao, and H. Zhang, Recent progress in chiral topological quantum interface, *Front. Phys.* **10**, 845579 (2022).
  - [8] G. J. Tang, X. T. He, F. L. Shi, J. W. Liu, X. D. Chen, and J. W. Dong, Topological photonic crystals: Physics, designs, and applications, *Laser Photonics Rev.* **16**, 2100300 (2022).
  - [9] M. Z. Hasan and C. L. Kane, *Colloquium*: Topological insulators, *Rev. Mod. Phys.* **82**, 3045 (2010).
  - [10] Y. Hatsugai, Chern number and edge states in the integer quantum Hall effect, *Phys. Rev. Lett.* **71**, 3697 (1993).
  - [11] F. D. Haldane and S. Raghu, Possible realization of directional optical waveguides in photonic crystals with broken time-reversal symmetry, *Phys. Rev. Lett.* **100**, 013904 (2008).
  - [12] Z. Wang, Y. D. Chong, J. D. Joannopoulos, and M. Soljacic, Reflection-free one-way edge modes in a gyromagnetic photonic crystal, *Phys. Rev. Lett.* **100**, 013905 (2008).
  - [13] S. A. Skirlo, L. Lu, and M. Soljacic, Multimode one-way waveguides of large Chern numbers, *Phys. Rev. Lett.* **113**, 113904 (2014).
  - [14] M. Hafezi, S. Mittal, J. Fan, A. Migdall, and J. M. Taylor, Imaging topological edge states in silicon photonics, *Nat. Photonics* **7**, 1001 (2013).
  - [15] B. Yang, T. Wu, and X. Zhang, Engineering topological edge states in two dimensional magnetic photonic crystal, *Appl. Phys. Lett.* **110**, 021109 (2017).
  - [16] B. Yang, H. Zhang, T. Wu, R. Dong, X. Yan, and X. Zhang, Topological states in amorphous magnetic photonic lattices, *Phys. Rev. B* **99**, 045307 (2019).
  - [17] A. B. Khanikaev, S. H. Mousavi, W. K. Tse, M. Kargarian, A. H. MacDonald, and G. Shvets, Photonic topological insulators, *Nat. Mater.* **12**, 233 (2013).
  - [18] L. H. Wu and X. Hu, Scheme for achieving a topological photonic crystal by using dielectric material, *Phys. Rev. Lett.* **114**, 223901 (2015).
  - [19] X. Cheng, C. Jouvaud, X. Ni, S. H. Mousavi, A. Z. Genack, and A. B. Khanikaev, Robust reconfigurable electromagnetic pathways within a photonic topological insulator, *Nat. Mater.* **15**, 542 (2016).
  - [20] C. He, X. C. Sun, X. P. Liu, M. H. Lu, Y. Chen, L. Feng, and Y. F. Chen, Photonic topological insulator with broken time-reversal symmetry, *Proc. Natl. Acad. Sci. USA* **113**, 4924 (2016).
  - [21] X. Wu, Y. Meng, J. Tian, Y. Huang, H. Xiang, D. Han, and W. Wen, Direct observation of valley-polarized topological edge states in designer surface plasmon crystals, *Nat. Commun.* **8**, 1304 (2017).
  - [22] Z. Gao, Z. Yang, F. Gao, H. Xue, Y. Yang, J. Dong, and B. Zhang, Valley surface-wave photonic crystal and its bulk/edge transport, *Phys. Rev. B* **96**, 201402(R) (2017).
  - [23] J. W. Dong, X. D. Chen, H. Zhu, Y. Wang, and X. Zhang, Valley photonic crystals for control of spin and topology, *Nat. Mater.* **16**, 298 (2017).
  - [24] X.-D. Chen, F.-L. Zhao, M. Chen, and J.-W. Dong, Valley-contrasting physics in all-dielectric photonic crystals: Orbital angular momentum and topological propagation, *Phys. Rev. B* **96**, 020202(R) (2017).
  - [25] T. Ma and G. Shvets, All-Si valley-Hall photonic topological insulator, *New J. Phys.* **18**, 025012 (2016).
  - [26] A. B. Khanikaev and G. Shvets, Two-dimensional topological photonics, *Nat. Photonics* **11**, 763 (2017).
  - [27] B. Yang, H. Zhang, Q. Shi, T. Wu, Y. Ma, Z. Lv, X. Xiao, R. Dong, X. Yan, and X. Zhang, Details of the topological state transition induced by gradually increased disorder in photonic Chern insulators, *Opt. Express* **28**, 31487 (2020).
  - [28] Z. Wang, Y. Chong, J. D. Joannopoulos, and M. Soljacic, Observation of unidirectional backscattering-immune topological electromagnetic states, *Nature (London)* **461**, 772 (2009).
  - [29] H.-C. Chan and G.-Y. Guo, Tuning topological phase transitions in hexagonal photonic lattices made of triangular rods, *Phys. Rev. B* **97**, 045422 (2018).
  - [30] Y. Wu, C. Li, X. Hu, Y. Ao, Y. Zhao, and Q. Gong, Applications of topological photonics in integrated photonic devices, *Adv. Opt. Mater.* **5**, 1700357 (2017).
  - [31] M. P. Makwana and R. V. Craster, Designing multidirectional energy splitters and topological valley supernetworks, *Phys. Rev. B* **98**, 235125 (2018).
  - [32] L. He, H. Y. Ji, Y. J. Wang, and X. D. Zhang, Topologically protected beam splitters and logic gates based on two-dimensional silicon photonic crystal slabs, *Opt. Express* **28**, 34015 (2020).

- [33] Y. Kang, X. Ni, X. Cheng, A. B. Khanikaev, and A. Z. Genack, Pseudo-spin-valley coupled edge states in a photonic topological insulator, *Nat. Commun.* **9**, 3029 (2018).
- [34] Y. Yang, X. Qian, L. Shi, X. Shen, Y. Wang, and Z. H. Hang, Observation and control of pseudospin switching in a finite-width topological photonic crystal, *Opt. Express* **30**, 5731 (2022).
- [35] B. Yan, Y. Peng, A. Shi, J. Xie, P. Peng, and J. Liu, Pseudo-spin-valley coupled topological states protected by different symmetries in photonic crystals, *Opt. Lett.* **47**, 2044 (2022).
- [36] G. Wei, Z. Liu, L. Wang, J. Song, and J.-J. Xiao, Coexisting valley and pseudo-spin topological edge states in photonic topological insulators made of distorted Kekulé lattices, *Photonics Res.* **10**, 999 (2022).
- [37] H. Zhang, L. Qian, C. Wang, C. Y. Ji, Y. Liu, J. Chen, and C. Lu, Topological rainbow based on graded topological photonic crystals, *Opt. Lett.* **46**, 1237 (2021).
- [38] W. Sui, Y. Zhang, Z. Zhang, H. Zhang, Q. Shi, Z. Lv, and B. Yang, Pseudospin topological phase transition induced by rotation operation in two-dimensional dielectric photonic crystal with  $C_6$  symmetry, *Opt. Commun.* **527**, 128972 (2023).
- [39] M. C. Rechtsman, J. M. Zeuner, Y. Plotnik, Y. Lumer, D. Podolsky, F. Dreisow, S. Nolte, M. Segev, and A. Szameit, Photonic Floquet topological insulators, *Nature (London)* **496**, 196 (2013).
- [40] L. J. Maczewsky, J. M. Zeuner, S. Nolte, and A. Szameit, Observation of photonic anomalous Floquet topological insulators, *Nat. Commun.* **8**, 13756 (2017).
- [41] S. Mukherjee, A. Spracklen, M. Valiente, E. Andersson, P. Ohberg, N. Goldman, and R. R. Thomson, Experimental observation of anomalous topological edge modes in a slowly driven photonic lattice, *Nat. Commun.* **8**, 13918 (2017).
- [42] Y. Yang, Y. F. Xu, T. Xu, H. X. Wang, J. H. Jiang, X. Hu, and Z. H. Hang, Visualization of a unidirectional electromagnetic waveguide using topological photonic crystals made of dielectric materials, *Phys. Rev. Lett.* **120**, 217401 (2018).
- [43] S. Peng, N. J. Schilder, X. Ni, J. van de Groep, M. L. Brongersma, A. Alu, A. B. Khanikaev, H. A. Atwater, and A. Polman, Probing the band structure of topological silicon photonic lattices in the visible spectrum, *Phys. Rev. Lett.* **122**, 117401 (2019).
- [44] S. Barik, H. Miyake, W. DeGottardi, E. Waks, and M. Hafezi, Two-dimensionally confined topological edge states in photonic crystals, *New J. Phys.* **18**, 113013 (2016).
- [45] M. Proctor, R. V. Craster, S. A. Maier, V. Giannini, and P. A. Huidobro, Exciting pseudospin-dependent edge states in plasmonic metasurfaces, *ACS Photonics* **6**, 2985 (2019).
- [46] X. Zhu, H.-X. Wang, C. Xu, Y. Lai, J.-H. Jiang, and S. John, Topological transitions in continuously deformed photonic crystals, *Phys. Rev. B* **97**, 085148 (2018).
- [47] B. A. Bernevig, T. L. Hughes, and S.-C. Zhang, Quantum spin Hall effect and topological phase transition in HgTe quantum wells, *Science* **314**, 1757 (2006).
- [48] W. Sui, Y. Zhang, Z. Zhang, H. Zhang, Z. Lv, Q. Shi, D. Zhang, and B. Yang, Unidirectional propagation of helical edge states via exciting pseudospin  $d$  states in two-dimensional photonic crystals, *Appl. Phys. Lett.* **122**, 111103 (2023).
- [49] J. Ma, C. Ouyang, L. Niu, Q. Wang, J. Zhao, Y. Liu, L. Liu, Q. Xu, Y. Li, J. Gu, Z. Tian, J. Han, and W. Zhang, Topological edge state bandwidth tuned by multiple parameters in two-dimensional terahertz photonic crystals with metallic cross structures, *Opt. Express* **29**, 32105 (2021).
- [50] See Supplemental Material at <http://link.aps.org/supplemental/10.1103/PhysRevB.109.195305> for details of band structures and topological properties of  $C_6$  and  $C_6$ -like symmetric PhCs, scattering cross sections of different prisms and tight-binding model of  $C_6$  symmetric and  $C_6$ -like symmetric PhCs, HESs in  $T_5$ - $N_5$ ,  $T_6$ - $N_6$  and  $T_0$ - $N_0$  interface structures, and HESs in  $T_{345}$ - $N_6$  and  $T_{45603}$ - $N_{365046}$  structures.